

GMOS-IFU spectroscopy of 167-317 (LV2) proplyd in Orion¹

M.J. Vasconcelos², A.H. Cerqueira² and H. Plana,

*LATO-DCET, Universidade Estadual de Santa Cruz, Rodovia Ilhéus-Itabuna, km 16
Ilhéus, Bahia, Brazil - CEP 45662-000
mjvasc@uesc.br, hoth@uesc.br, plana@uesc.br*

A.C. Raga

*Instituto de Ciencias Nucleares, UNAM, Ap. Postal 70-543, CU, D.F. 04510, México
raga@nucleares.unam.mx*

and

C. Morisset

*Instituto de Astronomía, UNAM, Ap. Postal 70-264, CU, D.F. 04510, México
morisset@astroscu.unam.mx*

ABSTRACT

We present high spatial resolution spectroscopic observations of the proplyd 167-317 (LV2) near the Trapezium cluster in the Orion nebula, obtained during the System Verification run of the Gemini Multi Object Spectrograph (GMOS) Integral Field Unit (IFU) at the Gemini South Observatory. We have detected 38 forbidden and permitted emission lines associated with the proplyd and its redshifted jet. We have been able to detect three velocity components in the profiles of some of these lines: a peak with a 28-33 km s⁻¹ systemic velocity that is associated with the photoevaporated proplyd flow, a highly redshifted component associated with a previously reported jet (which has receding velocities of about 80-120 km s⁻¹ with respect to the systemic velocity and is spatially distributed to the southeast of the proplyd) and a less obvious, approaching structure, which

¹Based on observations obtained at the Gemini Observatory, which is operated by the Association of Universities for Research in Astronomy, Inc., under a cooperative agreement with the NSF on behalf of the Gemini partnership: the National Science Foundation (United States), the Particle Physics and Astronomy Research Council (United Kingdom), the National Research Council (Canada), CONICYT (Chile), the Australian Research Council (Australia), CNPq (Brazil) and CONICET (Argentina).

²Current Address: ICN-UNAM, Ap. Postal 70-543, CU, D.F. 04510, México

may possibly be associated with a faint counter-jet with systemic velocity of (-75 ± 15) km s⁻¹. We find evidences that the redshifted jet has a variable velocity, with slow fluctuations as a function of the distance from the proplyd. We present several background subtracted, spatially distributed emission line maps and we use this information to obtain the dynamical characteristics over the observed field. Using a simple model and with the extinction corrected H α fluxes, we estimate the mass loss rate for both the proplyd photoevaporated flow and the redshifted microjet, obtaining $\dot{M}_{proplyd} = (6.2 \pm 0.6) \times 10^{-7}$ M $_{\odot}$ year⁻¹ and $\dot{M}_{jet} = (2.0 \pm 0.7) \times 10^{-8}$ M $_{\odot}$ year⁻¹, respectively.

Subject headings: ISM: clouds — ISM: individual(Orion Nebula, LV2, 167-317)

1. Introduction

The Orion Nebula (M42) is the most active site of star formation of the Orion Molecular Cloud and contains many young stars, among them the Trapezium cluster. Its high mass young stellar members generate an intense ultraviolet radiation field that photodissociates and photoionizes the nearby material. These mechanisms promote the appearance of some complex structures as the so-called proplyds (O’Dell & Wen 1994). Proplyds are low mass YSOs that are being exposed to an intense ultraviolet radiation field which renders them visible. In Orion, there are approximately 160 proplyds (Bally et al. 2000) which are being photoionized mainly by θ^1 Ori C, an O6 spectral type star. There are several objects that have been identified as being proplyds not only near the Trapezium cluster (Bally et al. 2000) but also in other star forming regions (like NGC 3372, Smith et al. 2003). Most of them share the same features: a bow-shaped head that faces the ionization source, a tail, that is primordially directed away from the source, a young star, that may (or not) be visible, and a disk, sometimes seen in silhouette against the HII region (e.g., O’Dell et al. 1993; O’Dell 1998; Bally et al. 2000; Smith et al. 2005). Early studies of these objects, however, were only able to determine their apparent ubiquity close to the θ^1 Ori C star, their high ionization level and, in later studies, the presence of high velocity structures (outflows) associated with these condensations (e.g., Laques & Vidal 1979; Meaburn 1988; Meaburn et al. 1993).

The proplyds are presently explained by a set of models which include a photoevaporated wind, an ionization front and a photoionized wind (Johnstone et al. 1998; Störzer & Hollenbach 1998; Henney & Arthur 1998; Bally et al. 1998; O’Dell 1998; Richling & Yorke 2000). Johnstone et al. (1998) proposed models in which far ultraviolet radiation (FUV) and extreme ultraviolet radiation (EUV) are responsible for the mass loss rates of the proplyds depending on the distance of the proplyd to the ionization source. For the proplyds situated

at intermediate distances from the ionizing star, FUV photons penetrate the ionization front and photodissociate and photoevaporate material from the accretion disk surface, generating a supersonic neutral wind that passes through a shock front before reaching the ionization front as a neutral, subsonic wind. At the ionization front, EUV photons ionize the wind, and the material is then reaccelerated to supersonic velocities. The interaction of this supersonic ionized wind with the star wind generates bow shocks seen in $H\alpha$ and in $[\text{O III}]\lambda 5007$ in some proplyds (Bally et al. 1998). For proplyds closer to the ionizing star, the ionization front reaches the disk surface, and the resulting wind is initially subsonic, becoming supersonic further out.

In general, the models cited above are able to explain the main observational features of the Orion proplyds. The region close to the ionization front is responsible for most of the emission of these objects. Störzer & Hollenbach (1998) have shown that heating and dissociation of H_2 can explain the observed $[\text{O I}]\lambda 6300$ emission at the disk surface (Bally et al. 1998). Bally et al. (2000) proposed that neutral gas compressed between the shock front and the ionization front can explain the $[\text{O III}]\lambda 5007$ emission seen near the ionization front in some objects. Henney & Arthur (1998) were able to reproduce the observed $H\alpha$ intensity profile of the proplyds in Orion in terms of accelerating photoevaporated flows. Numerical 2D HD simulations with a treatment of the radiative transfer (Richling & Yorke 2000) also reproduce the proplyd morphology and emission, although in this work the treatment of the diffuse radiation is somewhat simplified.

There are several open issues about these objects. One of them is related with the calculation of the mass loss rate of the proplyds, that is strongly model dependent and which may pose severe constraints on the age of the Orion proplyds (as well as for θ^1 Ori C). As the flux of FUV photons dissociates the molecules in the disk of the proplyds, the sub- or trans-sonic *wind* is accelerated at the proplyd’s ionization front (IF) (see Henney et al. 2002 for a discussion), leading to derived mass-loss rates of $\approx 8 \times 10^{-7} M_\odot \text{ yr}^{-1}$ which imply a short lifetime for these systems (Churchwell et al. 1987). It is hard to reconcile such short lifetimes with the fact that the region of the Trapezium cluster is populated by several proplyds. Improvements in both models and observational techniques have slightly reduced the calculated mass-loss rates for these systems, and Henney et al. (2002) find $\dot{M} = 8.2 \times 10^{-7} M_\odot \text{ yr}^{-1}$ for the 167-317¹ (LV2) proplyd, implying an age of less than 10^5 yr for θ^1 Ori C, and $\dot{M} \lesssim 1.5 \times 10^{-6} M_\odot \text{ yr}^{-1}$ for the 170-377, 177-341, 182-413, 244-440 proplyds (e.g., Henney & O’Dell 1999).

¹The proplyds mentioned in the present paper will be denoted following the O’Dell & Wen (1994) notation, that is based on the coordinate of the object.

It is presently known that many proplyds show, besides protostellar features such as accretion disks and a young low mass protostar, the presence of jets. Bally et al. (2000), in a survey carried out using the WFPC2 camera on the HST, find 23 objects which appear to have collimated outflows seen as one-sided jets or bipolar chains of bow shocks. Meaburn et al. (2002) also found kinematical traces of jets associated with LV5 (158-323) and GMR 15 (161-307). The proplyd 167-317 shows evidence of the existence of a collimated outflow, detected spectroscopically (Meaburn 1988; Meaburn et al. 1993; Henney et al. 2002). Until now, this outflow was detected as a one-sided jet, with a P.A. of 120° and a propagation velocity of about 100 km s^{-1} . Recently, Smith et al. (2005) and Bally et al. (2005), using the Wide Field Camera of the Advanced Camera for Surveys (ACS/WFC) on HST, found jets associated with silhouette disks in the outer regions of Orion.

In this work, we present the first Integral Field Unity (IFU) observation of a proplyd. The observed object is 167-317, one of the brightest proplyds of the Trapezium. We discuss one of the very first results from the Gemini Multi-Object Spectrograph, in its IFU mode (hereafter, GMOS-IFU), at the Gemini South Telescope. In §2, we present the observations and the steps to obtain a calibrated, clean datacube. In §3 we present the spectral analysis for the observed region of the 167-317 proplyd, as well as the observed lines and intensity maps. We use the observed line profiles to identify the outflows in the system. In §4, we present the discussion and the conclusions.

2. The observations and data reduction

The data were taken during the System Verification run of the GMOS-IFU at the Gemini South Telescope (GST), under the GS-2003B-SV-212 program, on 2004 February 26th and 27th. The science field of view (FOV) is $3''.5 \times 5''$ with an array of 1000 lenslets of $0''.2$. The sky is sampled with 500 lenses which are located $1'$ from the science FOV. We used the R831_G5322 grating in single slit mode, giving a sampling of 0.34 \AA per pixel ($\approx 15 \text{ km s}^{-1}$ per pixel at $\text{H}\alpha$) and a spectral coverage between $\simeq 5515 \text{ \AA}$ to $\simeq 7630 \text{ \AA}$. The spectral resolution (i.e., the instrumental profile) is $47 \text{ km s}^{-1} \lesssim \text{FWHM} \lesssim 63 \text{ km s}^{-1}$ (the FWHM decreasing with increasing wavelength). A field centered on the 167-317 proplyd has been observed with an exposure time of 300s. A 60 s exposure of the standard star the Hiltner 600 has also been taken in order to derive the sensitivity function.

The data were reduced using the standard Gemini IRAF v1.6 ² routines. An average

²IRAF is distributed by the National Optical Astronomy Observatories, which are operated by the Association of Universities for Research in Astronomy, Inc., under cooperative agreement with the National

bias image has been prepared using the GBIAS task. The extraction has been worked out using the GCAL flat and the response using the twilight flat. Spectra extraction has been performed and wavelength calibration done using an arc taken during the run. The 167-317 field and Hiltner 600 star have been processed in the same way. The sensitivity function derived from the standard star has been applied to the observed field. Finally, data cubes have been built using the GFCUBE routine. We maintain the IFU original resolution of $0''.2$ px^{-1} although an interpolation was performed in order to turn the IFU hexagonal lens shape into squared pixels.

Because some of the emission lines are very intense, it was not possible to eliminate cosmic rays using the standard GSCRREJ routine of the IRAF Gemini v1.6 package. In order to remove cosmic rays we have then programmed an IDL routine. This routine works directly on the data cube by taking out impacts that are above a certain convenient level calculated based on the mean intensity of nearby pixels. The cosmic ray is then eliminated doing a linear interpolation in the wavelength direction. With this procedure, it is possible to keep very intense lines and eliminate lower level cosmic ray impacts that could be misinterpreted as low emission lines.

Further manipulation of the cube, such as the production of channel maps, emission line maps, dispersion and velocity maps, have been done using Starlink ³, IDL routines and Fortran programs developed specially for this purpose.

The subtraction of the background emission from the proplyd spectrum is a very challenging task (Henney & O'Dell 1999). This problem arises since the background nebular emission is strongly inhomogeneous on an arc-second scale. In this work, we have used standard χ^2 -method in order to fit an intensity versus position plane in a semi-rectangular field located $\approx 1'' - 1''.5$ away from the peak proplyd emission in each of the individual velocity channel maps. We assure that we only take samples of the background avoiding the region of the proplyd. These planar fits to the nebular emission are then subtracted from the corresponding velocity channel maps. In Figure 1, we show the observed field, the object orientation in the plane of the sky, and also the region that defines our background (region 4, labeled as R4 in Figure 1). Region 4 (see Figure 1) contains 76 spectra which are used to define the background. This Figure also shows an internal box (labeled as R1, or region 1), for which we have defined an arbitrary xy -coordinate system limited by $1 \leq x \leq 11$ (in the East direction) and $1 \leq y \leq 17$ (in the North direction; see Figure 1). In the following sections, we show maps of spatially distributed physical variables that will be constrained

Science Foundation.

³See documentation at this website: <http://star-www.rl.ac.uk/>

to the limits defined by this box. The spatial positions inside this domain will be defined using the xy -coordinate system described above. Regions 2 and 3 (labelled as R2 and R3 in Figure 1) define, respectively, a region near the center of the 167-317 proplyd and a region which has a high-velocity, redshifted feature (see below).

3. Observational results: spectral line identification and high velocity features

3.1. The emission lines intensities and ratios

The lines that we identify in the spectra have already been reported in previous papers of the Orion Nebula (e.g., Baldwin et al. 2000). We select 4 different regions to measure the line intensities, namely, regions R1, R2, R3 and R4 (see Fig. 1 and §2 for the coordinate system definition).

Four spectra are then obtained by co-adding the spectra of the pixels included in each region. The spectrum of region 1 is the result of the sum of 187 pixels, for region 2 the sum of 6 pixels, region 3 represents the spectrum of a single pixel and region 4 the sum of 76 pixels. A set of 38 lines has been selected from a manual search for emission features in the spectrum integrated over the selected fields. The intensities of the emission lines are determined by fitting a flat continuum and integrating over the whole emission feature⁴. Then, a mean flux was obtained dividing the integrated flux by the total number of pixels of each region. Table 1 gives the list of the observed lines together with the mean flux of each region (after subtraction of the emission from the background, region R4) and the ratio to $H\alpha$ (normalized to $H\alpha = 100$). The fourth and eighth columns show the background emission and ratios to $H\alpha$, respectively, for each line. The mean fluxes are given in units of 10^{-15} erg cm⁻² s⁻¹ px⁻¹, and are not corrected for reddening. The absolute error of the mean flux is given in parentheses. This error was calculated taking into account the variations of the local continuum. The errors can be very large for the weaker lines. Also, the detection of spectral lines in region R3 is affected by the low signal to noise ratio. There are some lines which show stronger mean fluxes in the background, namely, the lines of Si III λ 5740, Si II λ 5979, [Ni II] λ 7378 and [Fe II] λ 7155 (see Table 1). These lines have low ionization potentials and are expected to appear mainly in regions of lower ionization degree. The lower line intensities within the proplyd indicate that these lines are mainly emitted by the background nebula, and that they are absorbed at least partially by the dust in the proplyd.

⁴The radial velocity range that defines the integration limits in each intensity line determination varies from line to line, since the FWHM changes with the wavelength (see §2).

In Figure 2, we show the full extracted spectra from the data cube, for regions R1 to R4 as defined in Figure 1. In this figure, the spectra for regions R1, R2, R3 and R4 are depicted from bottom to top in each diagram. The data shown here are not background subtracted. Most of the detected 38 lines can be clearly seen in the spectra. It is also evident that the S/N is higher in regions R1 and R4 (which is due to the increase of the pixel number of these regions). Here, a third order cubic spline was fitted to the continuum and then subtracted from the data. Because of the high order spline polynome subtraction, some minor variations are still present near the $H\alpha$ line.

Figure 3 depicts (for region R1), 2D-intensity maps of the lines $[N\ II]\lambda 5755$, $[N\ II]\lambda 6548$, $H\alpha$, $[N\ II]\lambda 6583$, $[He\ I]\lambda 7065$ and $[Ar\ III]\lambda 7135$, superimposed by line profiles. The data shown here are background subtracted, as described in §2. The line profiles can be better seen in Figure 4, in which we show the mean line profile for each line and for each of the regions R1, R2, R3 and R4, in the same diagram. As could be anticipated, the flux is more intense in region R2 (dotted line), where the proplyd is located, except for the $[N\ II]\lambda 6548$ line, which shows a stronger flux in region R3. For the $H\alpha$ and $[N\ II]\lambda 6583$ lines the emission of region R3 is more intense than the emission of region R1. For lines with good S/N, the presence of a redshifted feature starts to become clear. An analysis of the profile components will be given in more detail below.

In order to see how the spectra of the different lines change spatially, in Figure 5 we present an intensity *versus* position plot for the same lines shown in Figures 3 and 4. We show how the intensity of these lines changes along a diagonal line, that crosses region R1 passing through the pixel (3,4) (region R3) and through the centre of region R2. We note that there are 2 intensity maxima for the $H\alpha$, $[N\ II]\lambda 6583$ and $[N\ II]\lambda 6548$ lines, clearly showing in which lines region R3 is clearly visible (also see Figure 3).

3.2. High velocity features

We associate region R3 with the redshifted jet of the proplyd, although in Figure 9 we will show that the emission of the jet is not restricted only to this pixel. A redshifted jet associated with the 167-317 proplyd was previously detected, with a propagation velocity of $\approx 100\text{ km s}^{-1}$ (e.g., Henney et al. 2002). We have also detected this high velocity feature in our data. In order to see this, we examine the behaviour of the moments of the radial velocity distribution. These are the flux-weighted mean radial velocity $\langle v \rangle$, the flux-weighted rms width of the line Δv^2 and the skewness Δv^3 , that are given, respectively, by:

$$\langle v \rangle = \frac{1}{I} \cdot \int I_v v dv \quad (1)$$

$$\Delta v^2 = \frac{1}{I} \cdot \int I_v (v - \langle v \rangle)^2 dv \quad (2)$$

$$\Delta v^3 = \frac{1}{I} \cdot \int I_v (v - \langle v \rangle)^3 dv \quad (3)$$

where

$$I = \int I_v dv \quad (4)$$

The integrated intensity (see eq. 4 and Figure 3) shows that if we move away from the proplyd position (R2), the emission for several lines (for example, H α and [Ar III]) rapidly drops to low values (close to the background value). We also note that the maps for the flux-weighted mean radial velocity ⁵ (not shown here; see eq. 1) show that $\langle v \rangle = 50 \pm 20$ km s⁻¹.

The flux-weighted rms width of the line (Δv^2)^{1/2} and the skewness (Δv^3)^{1/3} moment of the radial velocity distribution (see equations 2 and 3, respectively) are depicted in Figure 6, for the H α (left) and [Ar III] (right) lines. Both of them were computed after carrying out both background and continuum subtractions. From Figure 6, we see that there is a clear enhancement of both of these moments from the proplyd position (R2 region) towards the R3 region (i.e., towards the SE direction, at a PA $\approx 135^\circ$). This behaviour of the moments leads us to infer that: 1) there is an increase in the line width as we go from the proplyd position to the SE direction; and 2) that there are redshifted wings in the line profiles. These results indicate the presence of a redshifted outflow in this region. We note that the same behaviour is seen in the He I $\lambda 6678.15$, [N II] $\lambda 6583.46$ lines (not shown here).

In order to confirm the presence of high velocity components in the observed field, as well as to see the behaviour of the photoevaporated proplyd flow and the background emission, we have computed three-component Gaussian minimum χ^2 fits for each position-dependent line profile. The profiles of all emission lines have a major peak at $v_{rad} = 40 - 60$ km s⁻¹,

⁵Unless explicitly mentioned, the radial velocities presented here are not corrected for the systemic radial velocity, that is of the order of $v_\odot \approx 26$ km s⁻¹ (e.g., Meaburn et al. 1993). The error in the radial velocity measurements is of the order of 2.5 km s⁻¹.

the exact radial velocity of this peak changing with spatial position. In some spectral lines, there is an evident second peak at redshifted velocities ranging from 100 to 150 km s⁻¹, corresponding to the jet associated with the proplyd. Finally, we have been able to detect a blueshifted component, which is fainter than the redshifted components. As an example of our three-component Gaussian fit, in Figure 7 we show the data (full line) and the fit (crosses), for the H α and [Ar III] λ 7135 lines in the $(x,y)=(6,7)$ position. In this figure, for each emission line, the top-left panel represents the data and the three Gaussian fits, the top-right panel shows the main, low velocity component (and the Gaussian fit for this component), the bottom-left panel depicts the data minus the main component together with the fits for the blue- and red-shifted components and, finally, the bottom-right panel shows the residual, obtained by subtracting the three-component fit from the observed line profile. The fits depicted in this figure show the presence of redshifted and blueshifted components. The redshifted component is present in several lines in pixels around the SE direction, as already mentioned before. On the other hand, blueshifted emission can be found in several pixels to the NW of the proplyd peak emission as can be seen in the left bottom panel of Figure 7 and this could represent the first spectroscopic determination of the presence of a blueshifted counter-jet, with systemic velocities of $-60 \text{ km s}^{-1} \lesssim v_{rad} \lesssim -90 \text{ km s}^{-1}$. This blueshifted component is also suggested by the fitted profiles of HeI λ 7065 (not shown here).

Figure 8 depicts the spatially distributed intensity over the R1 region (see Figure 1), of the main peak for the [N II] λ 5754 (top-left), [N II] λ 6548 (top-middle), H α (top-right), [N II] λ 6583 (bottom-left), HeI λ 7035 (bottom-middle) and [Ar III] λ 7135 (bottom-right) lines. The values shown in this Figure were obtained from three-component Gaussian fits to the observed line profile. All of the lines peak at the proplyd position, at $(x,y) = (6,7)$, inside the R2 region, and three of them (namely [N II] λ 6548, top-middle; H α , top-right; and [N II] λ 6583, bottom-left), have a secondary, less intense peak at $(x,y)=(3,4)$ (i.e., in the R3 region; see Figure 1 for the definition of the coordinate system). This secondary peak is probably related to the jet, since, as we have seen before, the jet propagates from the R2 region towards the SE direction. It is also interesting to note that there is a tail of faint emission (compared with the maximum in a given map) that extends in the NE direction, and that can be seen in both of the [N II] lines that bracket H α (top-middle and bottom-left maps in Figure 8).

In Figure 9, we show the spatially dependent intensity (Fig. 9a) and the central velocity (Fig. 9b) of the redshifted component of the fitted H α profile. We limit the maps to the spatial pixels which have a skewness $|(\Delta v^3)^{1/3}| > 30 \text{ km s}^{-1}$. The pixels which satisfy this criterium have a well defined high velocity, redshifted component. These figures show that the high velocity component has an intensity maximum near the center of the proplyd, with an extension towards the SE direction (along the jet axis), surrounded by a region of

decreasing fluxes. The high intensity spike seen in H α , [N II] λ 6548 and [N II] λ 6583 lines (Figure 3) can be seen here. The jet shows a spread in velocity values, although most of the pixels present velocities around 120-140 km s $^{-1}$. This figure also shows that the jet velocity decreases with increasing distance from the proplyd. This trend can be seen in the Figure 9c, where we show the radial velocity of the redshifted component as a function of distance from the proplyd position, $(x,y) = (6,7)$ in region R1. To build this figure, we assume that the jet is propagating in a PA $\approx 135^\circ$ position angle. We define a box with one axis aligned with the jet axis, and the second, perpendicular dimension extending two pixels to each side of the jet axis. We then take averages (of the mean velocity of the redshifted component) perpendicular to the jet direction and plot the resulting velocity as a function of distance from the proplyd (see the bottom frame of Figure 8). There is an indication that the jet velocity is slowly diminishing as a function of distance from the source.

3.3. The spatial distribution of the nitrogen ratio

In Figure 10a, we show a map for the R1 region of the line ratio:

$$\frac{[\text{N II}]\lambda 6548 + [\text{N II}]\lambda 6583}{[\text{N II}]\lambda 5754} = \frac{A_{6548}\sigma_{6548} + A_{6583}\sigma_{6583}}{A_{5754}\sigma_{5754}}, \quad (5)$$

where A and σ are the height and the dispersion of the fitted Gaussian profile (of the main, low velocity component). The [NII](6548+6583)/5754 ratio is a classical electron temperature diagnostic of low/medium density nebulae ($N_e < 10^5$ cm $^{-3}$). At high densities, due to the collisional desexcitations, this ratio cannot be used for the determination of the electron temperature, but it turns out to be a quite good electron density diagnostic. This can be seen, for example, from the Osterbrock (1989) equation:

$$[\text{NII}](6548 + 6583)/5754 = \frac{6.91 \exp(2.5 \times 10^4/T_e)}{1 + 2.5 \times 10^{-3}(N_e/T_e^{1/2})} \quad (6)$$

Figure 10b shows the lines corresponding to [NII](6548+6583)/5754 = 9, 10, 11, 80, 90, 100 in a $T_e - N_e$ plane. We can see that for the values obtained in our case (line ratios close to 10), the [NII](6548+6583)/5754 ratio is strongly dependent on the electron density, and that the dependence on the electron temperature is small.

In Figures 10c and 10d, we show the densities computed from the [NII](6548+6583)/5754 ratio for $T = 10^4$ K and $T = 1.5 \times 10^4$ K, respectively. Although presenting a very complicated pattern, these figures show that the region coinciding with the proplyd center, and

extending towards the SE direction (the jet propagation direction), shows the lowest line ratio, indicating electron densities (n_e) of the order of $2 \times 10^6 \text{ cm}^{-3}$. This value is at least in qualitative agreement with the $n_0 = (3.0 \pm 0.5) \times 10^6 \text{ cm}^{-3}$ obtained by Henney et al. (2002) considering a $T = 1.2 \times 10^4 \text{ K}$ temperature for the ionization front (that is inside the R2 region). We can also note that both figures are similar, presenting few differences in the density values.

The extended structure from the R2 region towards the SE direction is surrounded by a region in which the nitrogen line ratio reaches values of up to ≈ 30 . In this limit, $n_e < 10^5 \text{ cm}^{-3}$. It is interesting to note that in the clump associated with the redshifted jet, the nitrogen line ratio increases substantially, indicating a decrease in the electron density when compared with the same values near the center of the proplyd. We have also obtained the [S II] $\lambda 6716, \lambda 6730$ emission maps. Unfortunately, we are not able to use these lines as a diagnostic because neither the ratio of this doublet is a good electron density indicator for this case (since it is constant for densities higher than 10^5 cm^{-3}) nor do we have a good enough signal to noise ratio for these lines. Furthermore, the background subtracted spectra for these two lines give us negative fluxes in the proplyd region (see Table 1). The presence of these negative features in the line profiles is probably related with the presence of dust, as discussed by Henney & O’Dell (1999).

4. Discussion and conclusions

We have presented in this work the first Integral Field Unit (IFU) spectroscopic observations of a photoevaporating disk immersed in a HII region. In particular, we have taken advantage of the System Verification Run of the Gemini South Telescope Multi Object Spectrograph (GMOS) to obtain spectra of the 167-317 proplyd in the Orion nebula. The 167-317 proplyd, also known as LV2 (from the pioneering work from Laques & Vidal 1979), is one of the brightest and best studied proplyds. In a single exposure, we took 400 spectra with a spatial resolution of $0''.2$. These spectra have been combined in order to optimize this instrumental feature, and, before discussing of our results, we want to make a few comments concerning the potential use of such IFU data-cubes for these objects. As previously discussed in the literature (Henney et al. 2002), the subtraction of the background emission is a very challenging task. This problem arises since the background near these proplyds (which are immersed in a highly non-homogeneous, photoionized ambient medium) is very complex and changes in an arc-second spatial scale. A careful computation of the background contribution to the spectra of these objects is one of the most important tasks in order to have reliable radial velocity measurements for both the proplyd photoevaporated flow and the

high velocity features (jets) present in these systems. Here, we have used the 76 spectra, defined in Figure 1 as region R4, in order to obtain a planar fit for the background emission. We think that such a definition of the background emission is more precise, since we use several regions to calculate a better function to describe the background. One more thing to point out is that, with spatially distributed spectra, we are able to confidently separate the contribution of the background from the contribution of the object itself.

The data from the IFU observation of the 167-317 proplyd also allow us to investigate the spatially dependent properties of the outflows associated with this object. In particular, the 167-317 proplyd is known to have a redshifted, collimated jet that propagates with heliocentric velocities of $\approx 100 \text{ km s}^{-1}$ towards the SE direction, and with a spatial extension of $\sim 2''$ (e.g, Meaburn 1988; Meaburn et al. 1993; Massey & Meaburn 1995; Henney 2000; Henney et al. 2002). We find that a prominent, high velocity redshifted component can be detected in some emission lines, particularly in $\text{H}\alpha$, in this SE direction. The redshifted jet has a trend in its radial velocity (as a function of distance from the proplyd) with higher velocities close to the proplyd and lower velocities at increasing distances. We note that Henney et al. (2002) had previously suggested a variation in the jet velocity as a function of distance from the source.

There is a subtle peak (in several emission lines, particularly in $[\text{N II}]\lambda 5754$ and $\text{H}\alpha$) that is associated with the SE jet emission, and located at $\approx 0''.67$ SE of the center of the proplyd [at $(x,y)=(3,4)$; the R3 region in Figure 1]. For this intensity peak, and also using the $\text{H}\alpha$ profiles of the neighbouring pixels, we find a mean heliocentric velocity $v_{red} = 116 \pm 10 \text{ km s}^{-1}$. It is interesting to note that previous HST images and spectroscopic analyses (Bally et al. 2000; Henney et al. 2002) also reveal a spike in the jet emission at $\approx 0''.4$ from the proplyd cusp. If we associate these two emission regions as belonging to the same condensation, we can estimate a proper motion of $\simeq 140 \text{ km s}^{-1}$, which combined with the $\simeq 116 \text{ km s}^{-1}$ radial velocity give a full jet velocity of $\approx 180 \pm 90 \text{ km s}^{-1}$ (where the error was inferred from the spatial resolution of our data). This velocity is of the same order as the values inferred for Herbig-Haro jets associated with T Tauri stars. However, the exact nature of this spike is unknown. We could relate this spike with a bow shock of the jet, since the line profiles for both are similar (Hartigan et al. 1987; Beck et al. 2004), showing a low velocity, more intense peak together with a high velocity, less intense peak (similar to the line profiles seen in Figures 3, 4 and 7).

We have found evidence for a blueshifted component in several emission lines around the northwest tip of the proplyd position. In particular, the $\text{H}\alpha$ profiles reveal the presence of a blue-shifted component with systemic velocity $v_{blue} = (-75 \pm 15) \text{ km s}^{-1}$, which indicates that its velocity is similar though smaller than the one of the redshifted jet. However, the

intensities of the blue-shifted features are much lower than the intensity of the redshifted components associated with the SE jet: the counter-jet is at least four times less intense than the redshifted jet (in $H\alpha$). The presence of such a blue-shifted component very close to the LV2 proplyd, together with previously reported evidence that (at several arcseconds to the NW of this proplyd; see Massey & Meaburn 1995) there is a blueshifted component (in the [O III] λ 5007 line) strongly suggests the existence of a faint counterjet.

It is interesting to estimate the mass loss rate for the proplyd and the associated redshifted jet. In order to do this, we consider a simple model that assumes that the proplyd flow arises from a hemispherical, constant velocity wind that originates at the proplyd ionization front, at a radius r_0 . Using the $H\alpha$ luminosity $L_{H\alpha}$, we can then obtain the particle density n_0 at this point and the mass loss rate, from:

$$n_0 = \left(\frac{2L_{H\alpha} e^{\tau_{H\alpha}}}{4\pi\alpha_{H\alpha} h\nu_{H\alpha} r_0^3} \right)^{1/2}, \quad (7)$$

$$\dot{M} = 4\pi r_0^2 n_0 \mu m_H c_{II}, \quad (8)$$

where $e^{\tau_{H\alpha}}$ accounts for the extinction correction, $\alpha_{H\alpha} = 5.83 \times 10^{-14} \text{ cm}^3$ is the effective recombination coefficient for $H\alpha$, $h\nu_{H\alpha}$ is the energy of the $H\alpha$ transition, $\mu = 1.3$ is the mean molecular weight and $c_{II} = 10 \text{ km s}^{-1}$ is a typical value for the sound velocity in an HII region. The extinction correction is obtained from the base 10 logarithm of the extinction at $H\beta$ ($c_{H\beta}$) which for the proplyd 167-317 is equal to 0.83 (O'Dell 1998) through the relation, $c_{H\beta} = K\tau_{H\alpha}$ (O'Dell et al. 1992), where here we take $K = 0.56$. Assuming for the ionization front radius a value $r_0 = (7.9 \pm 0.2) \times 10^{14} \text{ cm}$ (Henney et al. 2002) we obtain $n_0 = (2.3 \pm 0.6) \times 10^6 \text{ cm}^{-3}$ and $\dot{M} = (6.2 \pm 0.6) \times 10^{-7} \text{ M}_\odot \text{ year}^{-1}$. Henney et al. (2002) have obtained a $\dot{M} = 8.2 \times 10^{-7} \text{ M}_\odot \text{ year}^{-1} \pm 10\%$, and the small differences between both results may arise from the different observational techniques employed in both cases.

For the redshifted jet, we assume that the outflow arises from the blob located in region R3 (or pixel 3,4). In this case, the particle density, mass and mass loss rate of the jet are given by,

$$n = \left(\frac{3L_{H\alpha}}{4\pi\alpha_{H\alpha} h\nu_{H\alpha} r_B^3} \right)^{1/2}, \quad (9)$$

$$M = \frac{4\pi}{3} r_B^3 n \mu m_H, \quad (10)$$

$$\dot{M} \sim M \frac{v_j}{L_j}, \quad (11)$$

where $r_B = 6.7 \times 10^{14}$ cm is the radius of the blob, $v_j = 180$ km s⁻¹ and $L_j = 4.5 \times 10^{15}$ cm are the propagation velocity and length of the jet, respectively, derived above. With these values, we obtain for the jet a mass loss rate equal to $(2.0 \pm 0.7) \times 10^{-8}$ M_⊙ year⁻¹, which is similar to the mass loss rate of typical HH jets from T Tauri stars.

We have been able to construct a ([NII]λ6548 + [NII]λ6583)/[NII]λ5754 line ratio map. This ratio indicates densities higher than 10⁵ cm⁻³ for the proplyd emission region, consistent with values previously reported in the literature. We find a subtle enhancement of this ratio in the region of the redshifted jet. Further observations of electron temperature and density diagnostic lines would allow a more accurate determination of the spatial dependence of these important parameters.

We thank the anonymous referee for his/her comments and suggestions, which have improved significantly the presentation of the paper. We are grateful to W. Henney for enlightning discussions. M.J.V. and A.H.C. would like to thank the staff of the Instituto de Ciencias Nucleares, UNAM, México, for their kind hospitality, as well as for partial financial support during our visit. We would like to thank Bryan Miller, Tracy Beck and Rodrigo Carrasco from the Gemini Observatory, and Bruno Castilho from LNA/CNPq, for help us in the early stages of IFU-data processing. The work of M.J.V., A.H.C. and H.P. was partially supported by the Bahia state funding agency (FAPESB), by the Universidade Estadual de Santa Cruz (UESC) and by the Milenium Institute (CNPq Project n. 62.0053/01-1-PADCT III/Milênio). This work was partially funded by the CONACYT grants 41320-F and 43103-F and the DGAPA (UNAM) grants IN112602 and IN111803.

REFERENCES

- Baldwin, J. A., Verner, E. M., Verner, D. A., Ferland, G. J., Martin, P. G., Korista, K. T., & Rubin, R. H. 2000, *ApJS*, 129, 229
- Bally, J., Sutherland, R.S., Devine, D., & Johnstone, D. 1998, *AJ*, 116, 293
- Bally, J., O’Dell, C.R., & McCaughrean, M.J., 2000, *AJ*, 119, 2919
- Bally, J., Licht, D., Smith, N., & Walawender, J. 2005, *AJ*, 129, 355
- Beck, T. L., Riera, A., Raga, A. C., & Aspin, C. 2004, *AJ*, 127, 408

- Churchwell, E., Felli, M., Wood, D.O.S., & Massi, M. 1987, ApJ, 321, 516
- Hartigan, P, Raymond, J., & Hartmann, L. 1987, ApJ, 316, 323
- Henney, W. J. 2000, Rev. Mex. Astron. Astrof. (Serie de Conferencias), 9, 198
- Henney, W.J., & Arthur, S.J., 1998, AJ, 116, 322
- Henney, W.J., & O’Dell, C.R., 1999, AJ, 118, 2350
- Henney, W.J., O’Dell, C.R., Meaburn, J., Garrington, S.T., & Lopez, J.A. 2002, ApJ, 566, 315
- Johnstone, D., Hollenbach, D., & Bally, J., 1998, ApJ, 499, 758
- Laques, P., & Vidal, J.L. 1979, A&A, 73, 97
- Massey, R.M., & Meaburn, J. 1995, MNRAS, 273, 615
- Meaburn, J. 1988, MNRAS, 233, 791
- Meaburn, J., Massey, R.M., Raga, A.C., & Clayton, C.A. 1993, MNRAS, 260, 625
- Meaburn, J., Graham, M. F., & Redman, M. P. 2002, MNRAS, 337, 327
- O’Dell, C.R. 1998, AJ, 115, 263
- O’Dell, C. R., Wen, Z., & Hu, X. 1993, ApJ, 410, 696
- O’Dell, C. R., & Wen, Z. 1994, ApJ, 436, 194
- O’Dell, C. R., Walter, D. K., & Dufour, R. J. 1992, ApJ, 399, L67
- Osterbrock, D.E. 1989, in *Astrophysics of Gaseous Nebulae and Active Galactic Nuclei* (Univ. Science Books: Mill Valley, California)
- Richling, S., & Yorke, H. W. 2000, ApJ, 539, 258
- Smith, N., Bally, J., & Morse, J.A. 2000, ApJ, 587, L105
- Smith, N., Bally, J., Licht, D., & Walawender, J. 2005, AJ, 129, 382.
- Störzer, H., & Hollenbach, D. 1998, ApJ, 502, L71

Table 1: Detected emission lines for 167-317

Ion	Line $\lambda(\text{\AA})$	Mean Flux ($\times 10^{-15}$ erg cm $^{-2}$ s $^{-1}$ px $^{-1}$)				Line ratio ($H\alpha = 100$)			
		R1 ^a	R2	R3	R4	R1	R2	R3	R4
[Cl III]	5537.70	- ^b	0.024 (0.007) ^c	-	0.155 (0.007)	-	0.012 (0.003)	-	0.164 (0.007)
N II	5666.63	0.024 (0.004)	0.033 (0.003)	ND ^d	0.007 (0.003)	0.058 (0.009)	0.016 (0.002)	ND	0.007 (0.003)
N II	5679.56	-	0.002 (0.004)	ND	0.012 (0.004)	-	0.001 (0.002)	ND	0.012 (0.004)
Si III	5739.73	-	-	ND	0.038 (0.002)	-	-	ND	0.040 (0.002)
[N II]	5754.59	0.535 (0.003)	2.50 (0.01)	0.638 (0.004)	0.186 (0.003)	1.283 (0.008)	1.245 (0.005)	0.598 (0.004)	0.196 (0.003)
He I	5875.64	1.451 (0.003)	7.80 (0.01)	1.39 (0.03)	4.327 (0.001)	3.48 (0.01)	3.879 (0.008)	1.30 (0.03)	4.568 (0.005)
O I	5958.60	0.007 (0.003)	0.033 (0.007)	ND	0.013 (0.003)	0.016 (0.008)	0.016 (0.004)	ND	0.013 (0.003)
Si II	5978.93	-	-	ND	0.028 (0.002)	-	-	ND	0.030 (0.002)
O I	6046.44	0.014 (0.002)	0.09 (0.01)	ND	0.020 (0.001)	0.034 (0.004)	0.045 (0.005)	ND	0.021 (0.001)
[O I]	6300.30	0.306 (0.004)	1.58 (0.02)	0.38 (0.02)	0.086 (0.001)	0.73 (0.01)	0.78 (0.01)	0.35 (0.02)	0.091 (0.002)
[S III]	6312.06	0.44 (0.02)	2.11 (0.08)	0.29 (0.04)	0.516 (0.006)	1.05 (0.04)	1.05 (0.04)	0.28 (0.04)	0.545 (0.006)
Si II	6347.11	-	0.03 (0.01)	ND	0.063 (0.004)	-	0.015 (0.005)	ND	0.066 (0.004)
[O I]	6363.78	0.09 (0.01)	0.51 (0.02)	0.03 (0.03)	0.03 (0.01)	0.21 (0.03)	0.25 (0.01)	0.03 (0.02)	0.03 (0.01)
Si II	6371.37	-	0.03 (0.01)	ND	0.026 (0.003)	-	0.018 (0.007)	ND	0.027 (0.003)
[N II]	6548.05	1.00 (0.01)	2.55 (0.02)	2.53 (0.04)	3.475 (0.009)	2.39 (0.03)	1.27 (0.01)	2.34 (0.04)	3.67 (0.01)
H I	6562.82	41.73 (0.02)	201.20 (0.05)	106.66 (0.02)	94.73 (0.01)	100.0 (0.4)	100.0 (0.1)	100.0 (0.1)	100.0 (0.1)
C II	6578.05	0.02 (0.01)	0.10 (0.02)	0.05 (0.01)	0.09 (0.01)	0.04 (0.03)	0.05 (0.01)	0.05 (0.01)	0.09 (0.01)
[N II]	6583.45	3.134 (0.005)	8.48 (0.02)	5.304 (0.007)	10.710 (0.001)	7.51 (0.03)	4.21 (0.01)	4.972 (0.009)	11.30 (0.01)
He I	6678.15	0.530 (0.007)	2.621 (0.009)	0.42 (0.02)	1.241 (0.007)	1.27 (0.02)	1.303 (0.005)	0.40 (0.02)	1.310 (0.008)
[S II]	6716.44	0.016 (0.005)	0.029 (0.006)	-	0.425 (0.003)	0.04 (0.01)	0.015 (0.003)	-	0.448 (0.004)
[S II]	6730.82	0.044 (0.002)	0.06 (0.02)	-	0.945 (0.002)	0.107 (0.006)	0.032 (0.008)	-	0.998 (0.002)
He I	6989.48	-	0.016 (0.002)	ND	0.005 (0.000) ^e	-	0.008 (0.001)	ND	0.005 (0.000) ^e
O I	7002.12	0.014 (0.004)	0.088 (0.005)	0.01 (0.01)	0.022 (0.001)	0.03 (0.01)	0.044 (0.003)	0.01 (0.01)	0.023 (0.001)
He I	7065.18	0.995 (0.004)	5.393 (0.009)	0.39 (0.03)	2.439 (0.001)	2.38 (0.01)	2.680 (0.005)	0.37 (0.03)	2.574 (0.003)
[Ar III]	7135.79	3.713 (0.004)	19.39 (0.02)	1.88 (0.01)	5.277 (0.003)	8.90 (0.04)	9.64 (0.01)	1.76 (0.01)	5.570 (0.007)
[Fe II]	7155.16	-	0.06 (0.03)	ND	0.005 (0.005)	-	0.03 (0.01)	ND	0.005 (0.006)
He I	7160.60	0.003 (0.004)	0.007 (0.008)	ND	0.017 (0.004)	0.006 (0.009)	0.004 (0.004)	ND	0.018 (0.004)
C II	7231.33	0.004 (0.005)	0.04 (0.01)	ND	0.046 (0.004)	0.01 (0.01)	0.019 (0.005)	ND	0.049 (0.004)
[C II]	7236.42	0.024 (0.004)	0.140 (0.005)	-	0.108 (0.004)	0.06 (0.01)	0.070 (0.002)	-	0.115 (0.004)
O I	7254.45	0.028 (0.001)	0.17 (0.01)	ND	0.027 (0.001)	0.066 (0.003)	0.086 (0.007)	ND	0.028 (0.001)
He I	7281.35	0.13 (0.01)	0.73 (0.02)	0.04 (0.04)	0.235 (0.007)	0.32 (0.02)	0.365 (0.008)	0.03 (0.03)	0.248 (0.008)
He I	7298.05	0.006 (0.004)	0.040 (0.007)	ND	0.020 (0.001)	0.01 (0.01)	0.020 (0.003)	ND	0.021 (0.001)
[O II]	7319.99	3.94 (0.04)	21.9 (0.2)	2.032 (0.008)	1.488 (0.004)	9.4 (0.1)	10.89 (0.09)	1.905 (0.008)	1.571 (0.005)
[O II]	7330.30	2.99 (0.08)	16.38 (0.08)	1.45 (0.08)	1.12 (0.08)	7.2 (0.2)	8.14 (0.04)	1.36 (0.07)	1.18 (0.08)
[Ni II]	7377.83	0.003 (0.001)	ND	ND	0.013 (0.000) ^e	0.007 (0.002)	ND	ND	0.014 (0.000) ^e
[N I]	7442.00	0.005 (0.003)	0.024 (0.009)	ND	0.008 (0.003)	0.012 (0.008)	0.012 (0.004)	ND	0.008 (0.004)
[N I]	7468.31	0.009 (0.002)	0.049 (0.007)	ND	0.011 (0.001)	0.022 (0.004)	0.024 (0.003)	ND	0.012 (0.001)
[C II]	7530.00	0.012 (0.000) ^e	0.014 (0.001)	ND	0.010 (0.000) ^e	0.030 (0.001)	0.007 (0.000) ^e	ND	0.011 (0.000) ^e

^a The regions R1, R2, R3 and R4 are defined in Figure 1.^b The symbol - implies that $I_{\text{region}} - I_{\text{background}} < 0$.^c The terms inside the parentheses are the absolute errors of the intensity of each line, for each one of the regions.^d The symbol ND implies that the line were not detected in that region.^e Absolute error smaller than 6×10^{-4} .

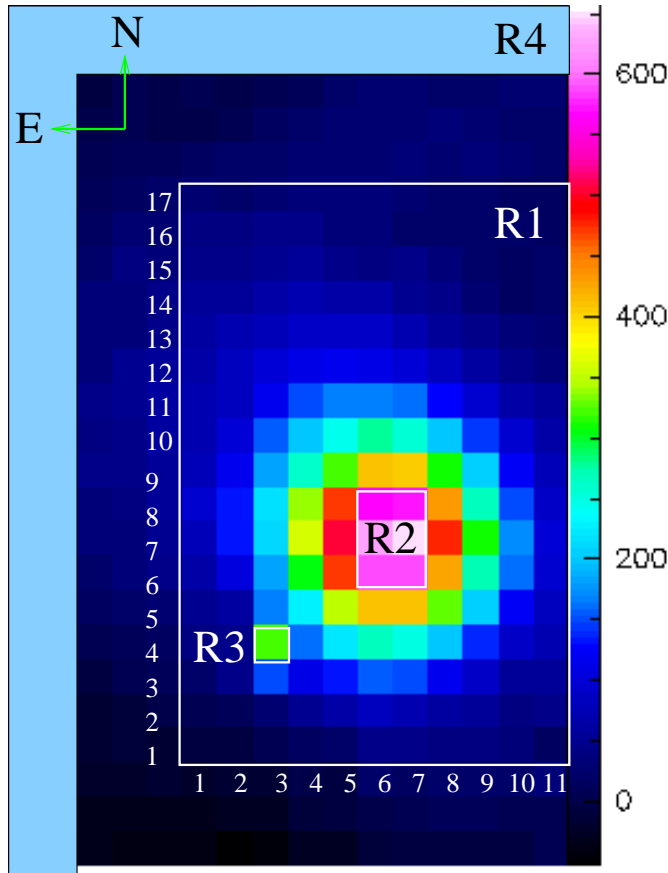


Fig. 1.— An $H\alpha$ integrated emission map (shown with a linear grey scale in arbitrary units) showing the location of the 167-317 proplyd with respect to the scientific field of view (SFOV), and its orientation: North is up and East is left, as indicated by the arrows on the top-left corner of the figure. The field has 16 pixels in the East direction and 25 in the North direction. The R4 frame located at the left and top parts of the figure represents the region chosen to define the background, which covers two columns of pixels on both the North and East directions. An internal box (R1), approximately centered on the object emission defines a coordinate system, and the numbers on the bottom axis and on the left axis of this internal box are referred to in the text as the x - and y -coordinates, respectively. This spatial sub-sample of spectra will be used throughout the paper. The θ^1 Ori C star is located at $7''.8$ from the proplyd, at a P.A. = 236° . Four regions are defined in this figure, namely R1 (the internal box), R2 (the proplyd center), R3 (a clump associated with a redshifted jet) and R4 (the background). We will refer to these regions throughout the paper.

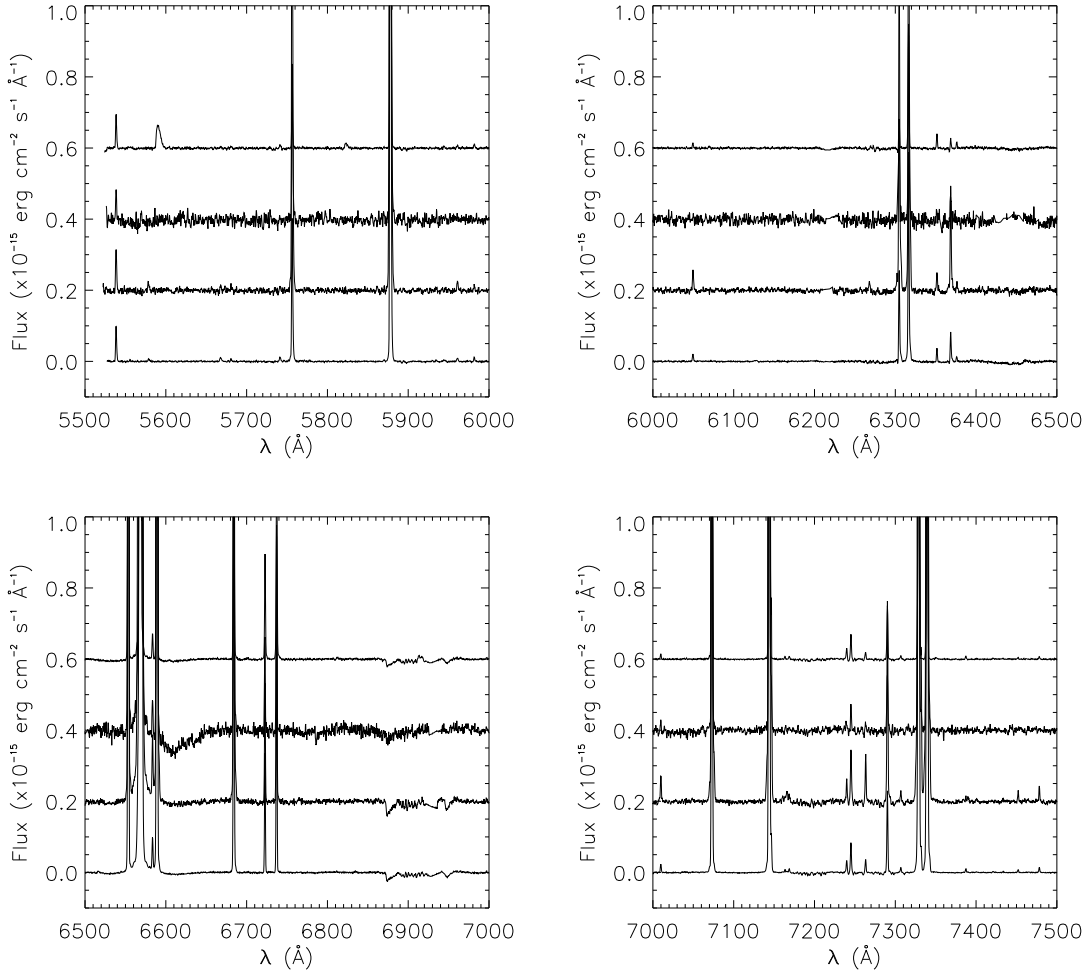


Fig. 2.— In each diagram, from bottom to top, are depicted, respectively, the spectra for regions R1, R2, R3 and R4. A 3rd order cubic spline was fitted in order to subtract the continuum and a constant n has been added to the spectra of regions R2 ($n = 0.2$), R3 ($n = 0.3$) and R4 ($n = 0.4$) in order to produce an intensity offset between the successive spectra. Wavelengths (λ) are in \AA , and the fluxes are in units of $10^{-15} \text{ erg cm}^{-2} \text{ s}^{-1} \text{ \AA}^{-1}$.

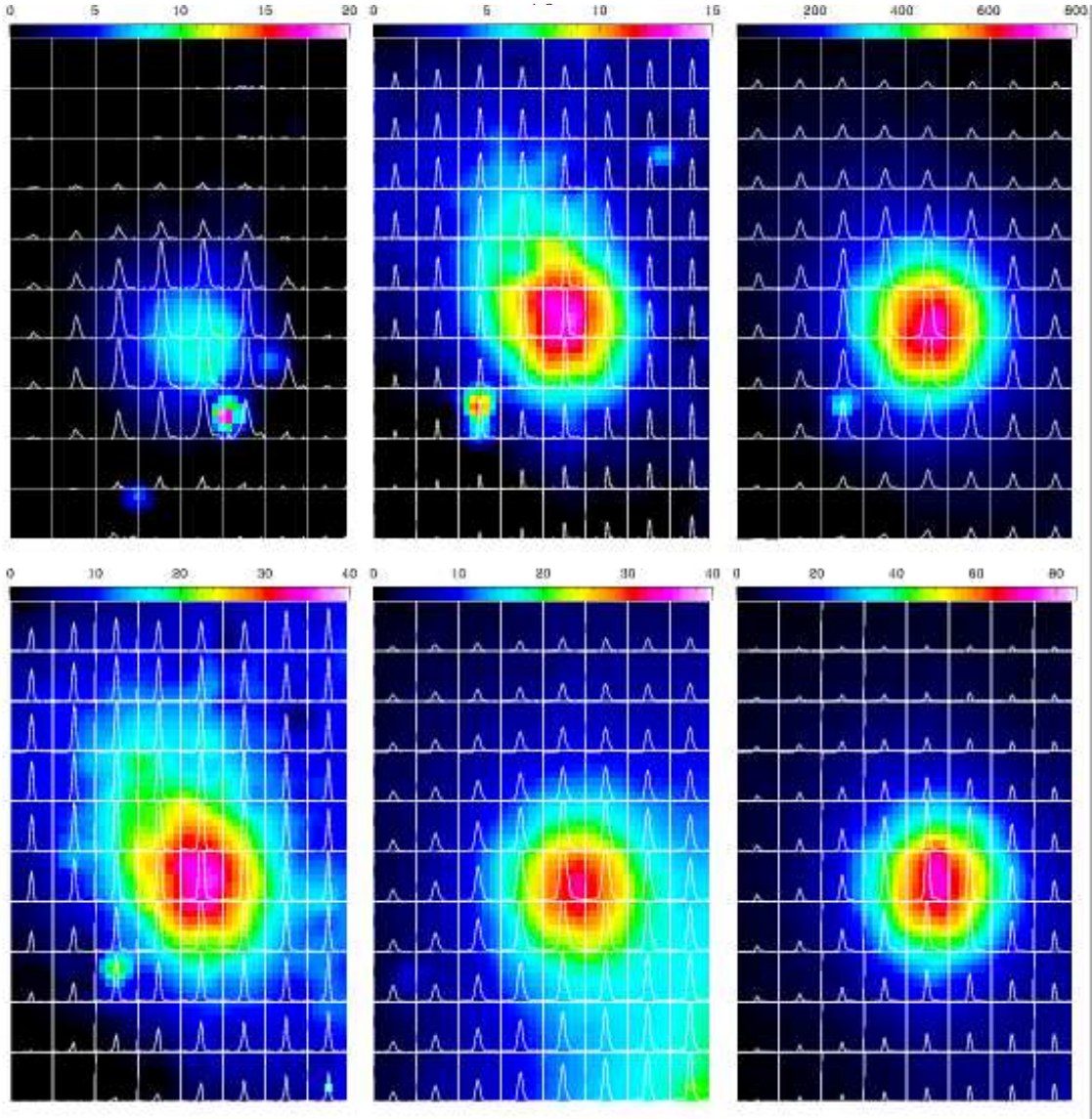


Fig. 3.— A sub-sample of the observed FOV, namely, the R1 region (see Figure 1), showing the integrated flux (the grey-scale map) for the following lines: [N II] λ 5755 (top-left), [N II] λ 6548 (top-center), H α (top-right), [N II] λ 6583 (bottom-left), [He I] λ 7065 (bottom-center) and [Ar III] λ 7135 (bottom-right). The linear bars give the grey-scale in unit of 1×10^{-15} erg cm $^{-2}$ s $^{-1}$ px $^{-1}$. The spectra in each position was background subtracted. Superimposed on the intensity maps are the line profiles for each box. See the text for a discussion. The orientation is the same as in Figure 1 (i.e., North is up and East is left). The original pixels (see Figure 1) have been resampled in order to smooth the emission features, and each box in these panels are slightly larger than the original pixels in Fig. 1.

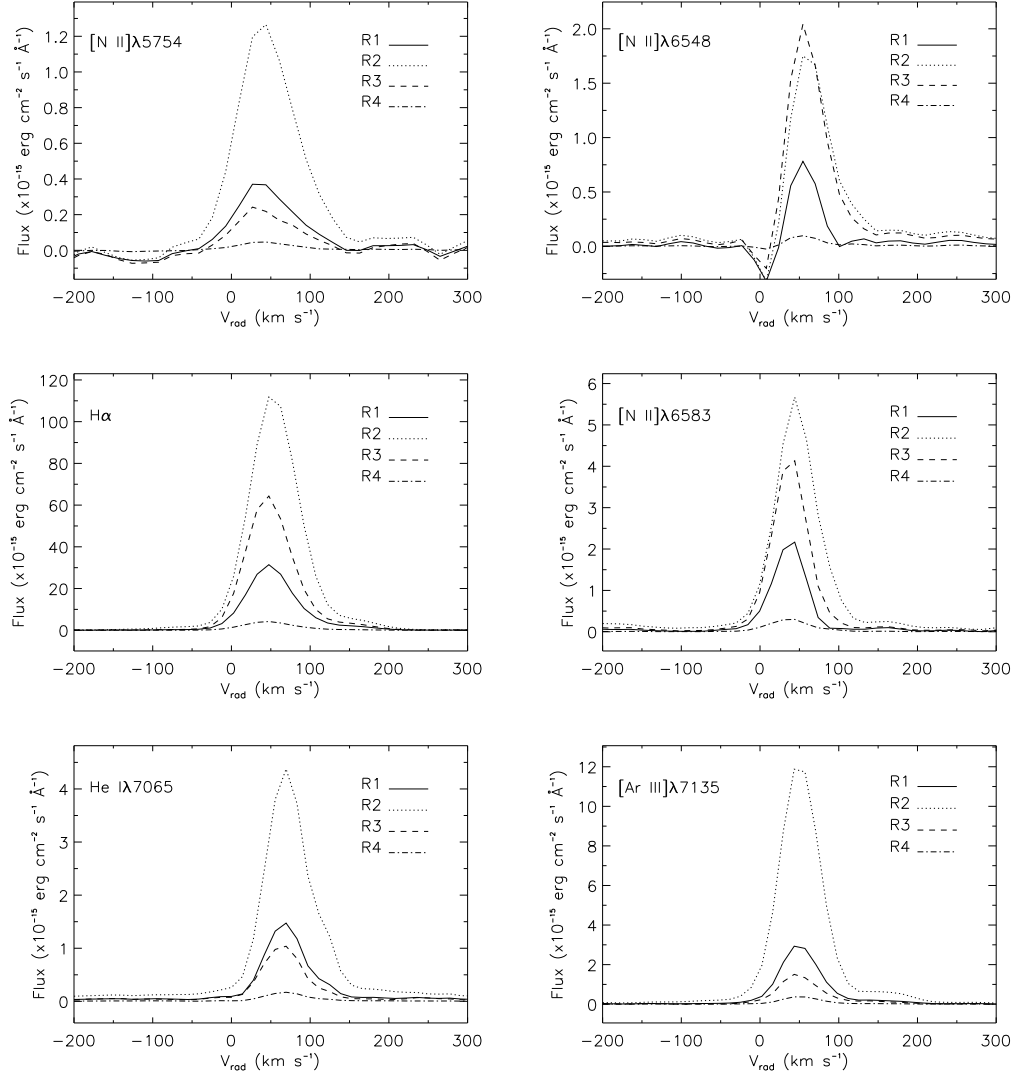


Fig. 4.— An alternative view of the line profiles depicted in Figure 3. Each diagram shows the line profile for regions R1 (continuous line), R2 (dotted line), R3 (dashed line) and R4 (dash-dotted line). The emission line is indicated on the top-left corner of each plot. The fluxes are in units of $1 \times 10^{-15} \text{ erg cm}^{-2} \text{ s}^{-1} \text{ per \AA}$ and they are plotted against the radial velocity (in units of km s^{-1} ; not corrected for the heliocentric velocity).

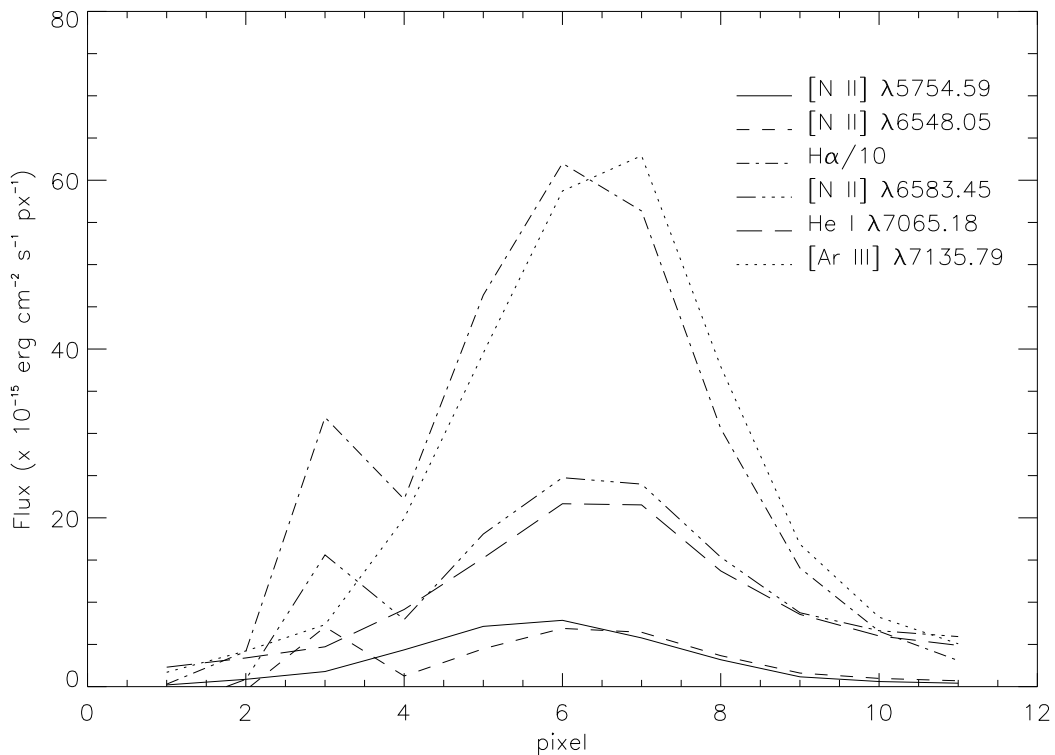


Fig. 5.— Intensity of the same lines depicted in Figure 3 as a function of the pixel position along a diagonal line that crosses region R1, beginning at pixel (1,2), passing through region R3 (pixel 3,4) and finishing at pixel (11,12). Each type of line shows the intensity of a different spectral line: the solid line shows [N II] $\lambda 5754$; the short dashed line, the intensity of [N II] $\lambda 6548$; the dot-dashed line, H α ; the triple dotted-dashed line, [N II] $\lambda 6583$; the long dashed line, He I $\lambda 7065$ and, finally, the dotted line shows [Ar III] $\lambda 7135$. In order to show all of the intensities in the same plot, we have divided the H α intensity by a factor of 10.

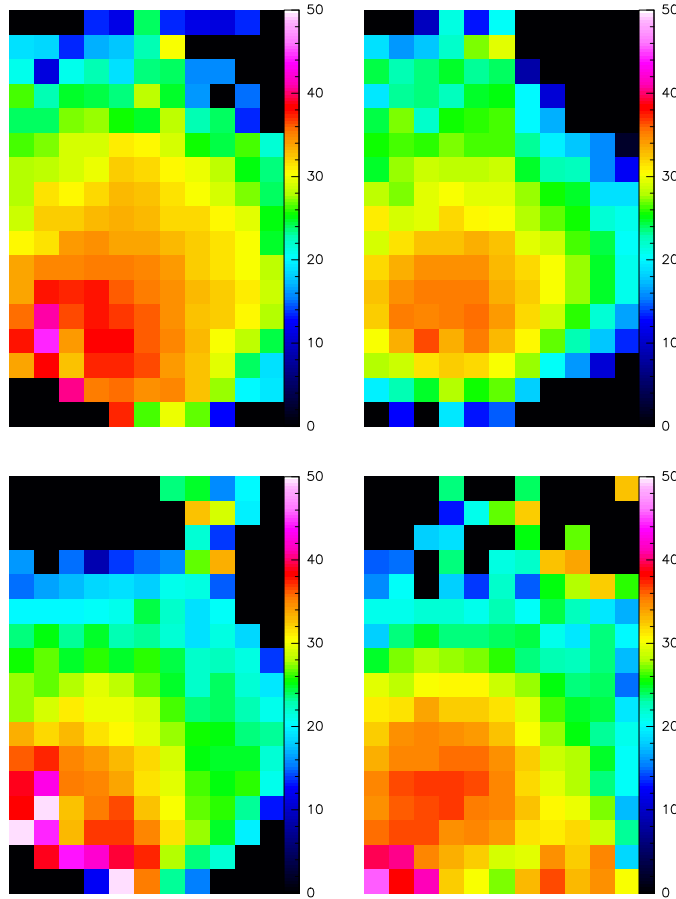


Fig. 6.— The flux-weighted rms width (top) and skewness (bottom) moments of the intensity vs. velocity distribution, as given by equations (2) and (3), respectively, for the $H\alpha$ (left) and $[\text{Ar III}]\lambda 7135.8$ (right) lines. The grey scale on the right side of each map is in unit of km s^{-1} . We note that both integrals show positive values and peak in a SE region, indicating the presence of a redshifted component towards the SE direction. The velocities are not corrected by the systemic radial velocity, and the integration limits in all maps are from $0 \leq v_{rad} \leq 200 \text{ km s}^{-1}$. The white pixels have values close to zero.

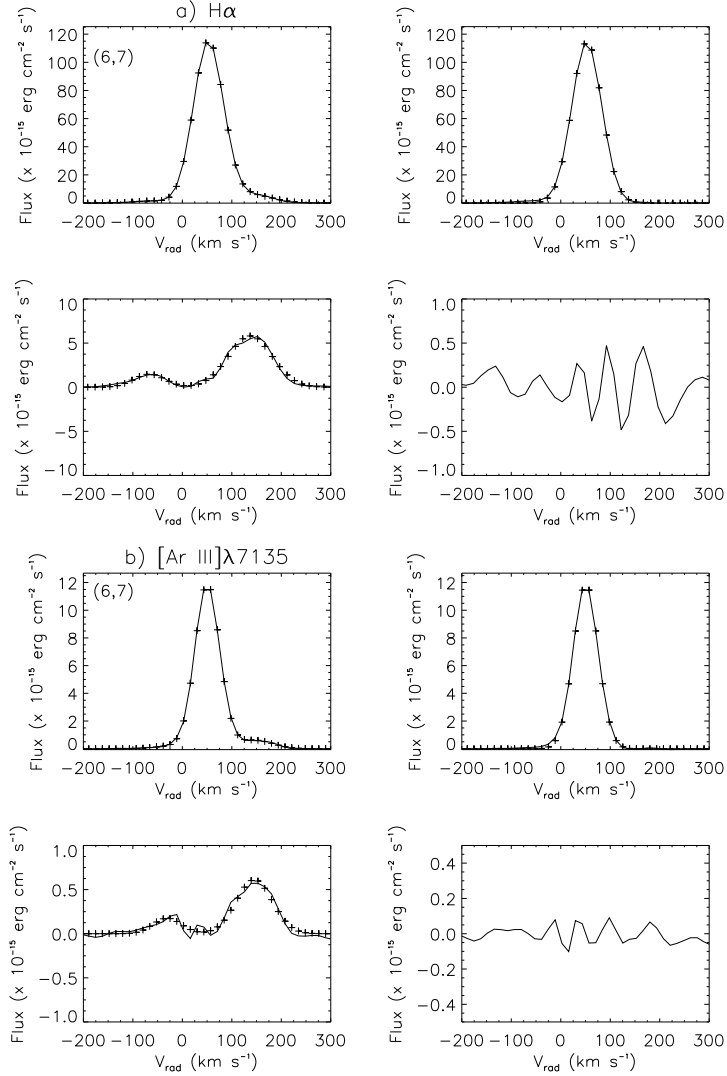


Fig. 7.— a) Background and continuum subtracted data (full line) together with the Gaussian fit (crosses) for the H α line at position $(x,y)=(6,7)$ (see Figure 1). *Top – left* : Line profile and the three Gaussian fit. *Top – right* : Main, low velocity line profile and its Gaussian fit. *Bottom – left* : The data profile subtracted from the main fitted profile, showing evidence for a blue- and a red-shifted component. *Bottom – right* : The data profile subtracted from the three-component Gaussian fit. The residual profile is a random fluctuation around a flux of 0.5×10^{-15} erg cm $^{-2}$ s $^{-1}$. These fluctuations corresponds to 10% of the flux for the blueshifted component, 0.5% of the flux for the main component and 10% of the flux for the redshifted component. b) The same but for the [Ar III] λ 7135 line.

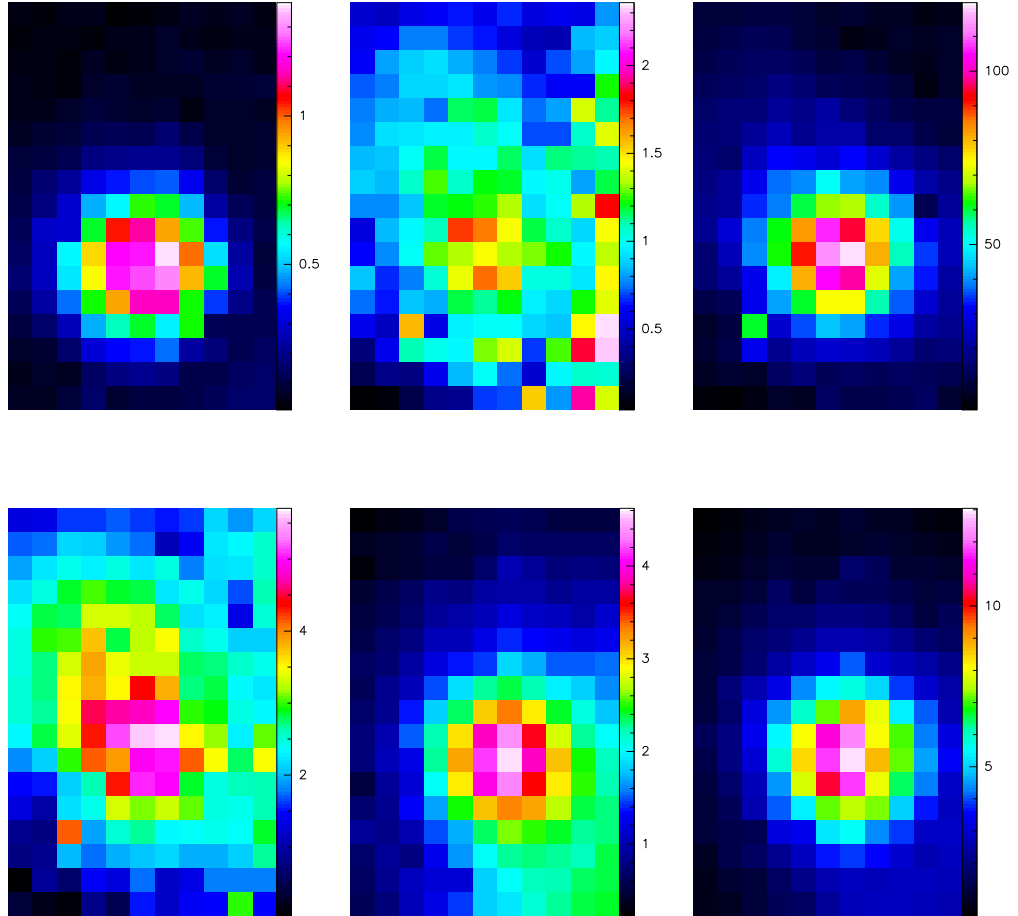


Fig. 8.— The intensity of the main, low velocity peak (in units of $1 \times 10^{-15} \text{ erg cm}^{-2} \text{ s}^{-1} \text{ px}^{-1}$) as a function of position for the [N II]λ5754 (top-left), [N II] λ6548 (top-center), Hα (top-right), [N II]λ6583 (bottom-left), HeI λ6678 (bottom-center) and [Ar III]λ7135 (bottom-right) lines. Almost all of the lines peak at the proplyd position, and three of them, namely the [N II]λ6548 (top-centre), Hα (top-right) and [N II]λ6583 (bottom-left lines), have a secondary, less intense peak in region R3 (see Figure 1).

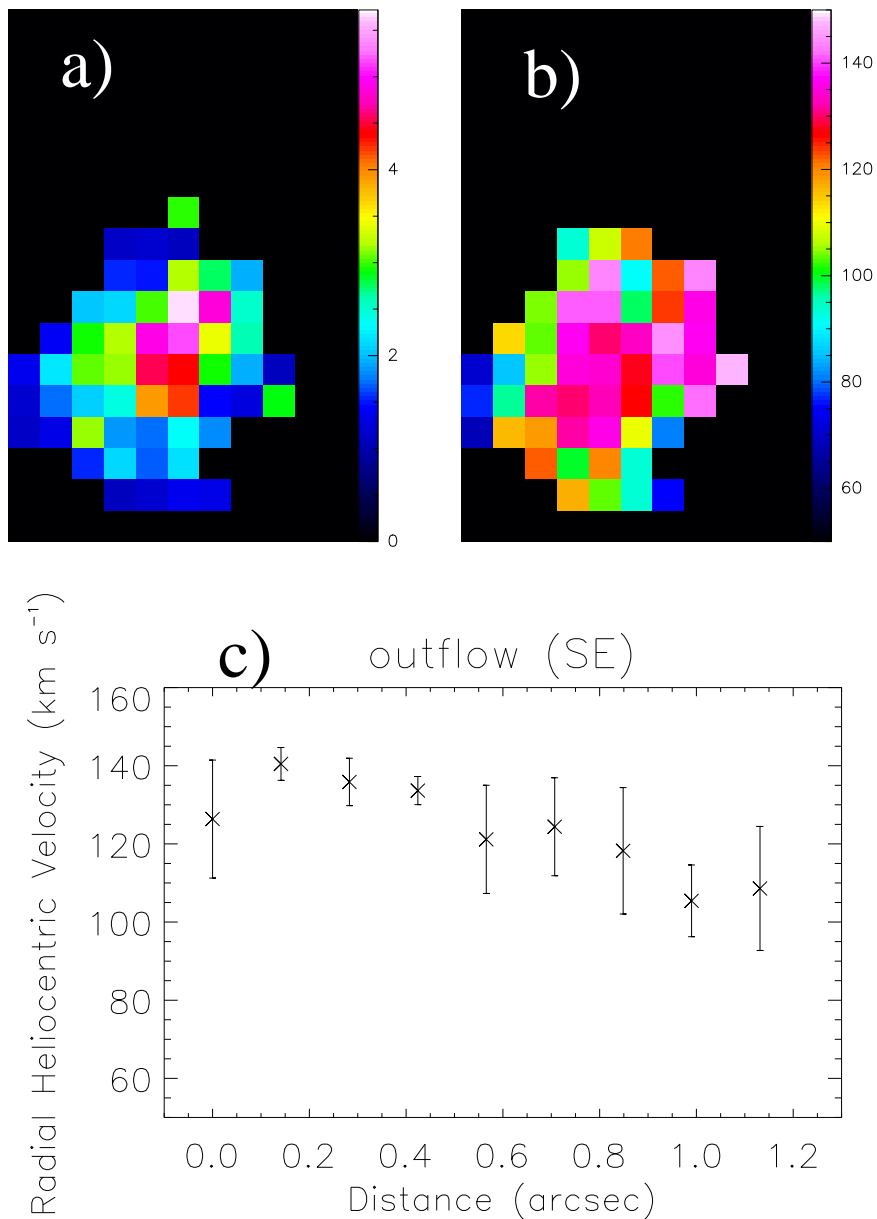


Fig. 9.— a) The intensity, in units of $1 \times 10^{-15} \text{ erg cm}^{-2} \text{ s}^{-1} \text{ px}^{-1}$, as a function of position in region R1. b) The velocity, in km s^{-1} for the redshifted Gaussian fit to the $\text{H}\alpha$ profiles. c) The jet velocity variation as a function of distance from the proplyd (see the text for a discussion). The velocities take into account the systemic radial velocity of $v_{\odot} \approx 26 \text{ km s}^{-1}$. The error associated with the radial velocity measurement is of the order of 2.5 km s^{-1} (see the text for a discussion).

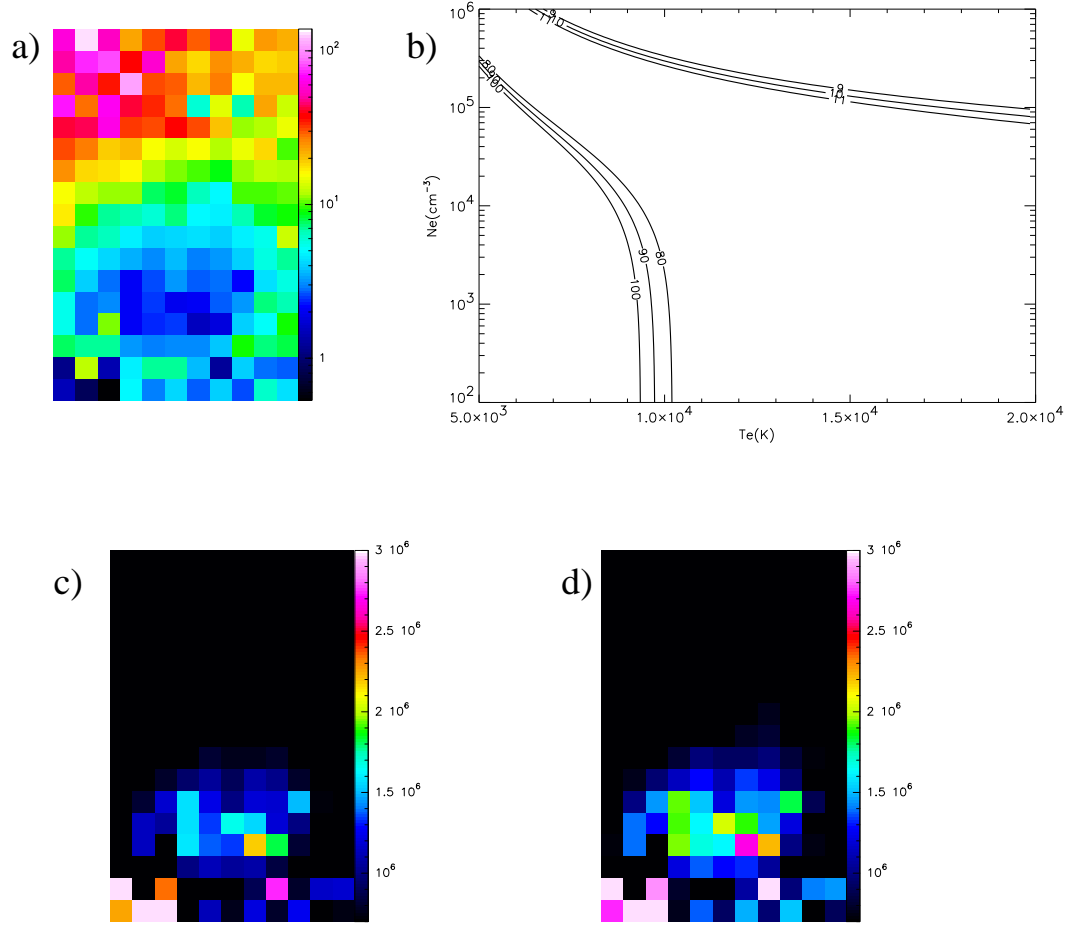


Fig. 10.— *a*) $N = ([\text{NII}]\lambda 6548 + [\text{NII}]\lambda 6583) / [\text{NII}]\lambda 5754$ ratio map of region R1 (see Figure 1) of the observed field. *b*) A $[T_e, n_e]$ diagnostic diagram showing the loci corresponding to different values of the nitrogen line ratio. *c*) The density for an assumed temperature of $T = 10^4$ K. *d*) The density for an assumed temperature of $T = 1.5 \times 10^4$ K.